Journal of
Applied Physics

RESEARCH ARTICLE | FEBRUARY 23 2026

Microsecond carrier lifetime measurement using extended time-resolved THz spectroscopy

K. M. Ashikur Rahman ; Bin Yun ; Jack L. Root ; George A. Blinick; Meng-Ju Sher

J. Appl. Phys. 139, 083101 (2026)
https://doi.org/10.1063/5.0311181

Articles You May Be Interested In

Microsecond carrier recombination times in InAs/AlAs quantum dots

Appl. Phys. Lett. (September 2002)

Microwave photoconductivity decay characterization of high-purity 4 H - Si C substrates

J. Appl. Phys. (July 2007)

Recombination and localization: Unfolding the pathways behind conductivity losses in $Cs_2AgBiBr_6$ thin films

Appl. Phys. Lett. (September 2021)

AIP Publishing

Journal of Applied Physics ARTICLE pubs.aip.org/aip/jap

Microsecond carrier lifetime measurement using extended time-resolved THz spectroscopy

Cite as: J. Appl. Phys. **139**, 083101 (2026); doi: 10.1063/5.0311181
Submitted: 7 November 2025 · Accepted: 30 January 2026 ·
Published Online: 23 February 2026

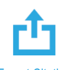

K. M. Ashikur Rahman, Bin Yun, Jack L. Root, George A. Blinick, and Meng-Ju Sher[a)]

AFFILIATIONS

Department of Physics, Wesleyan University, Middletown, Connecticut 06459, USA

Note: This paper is part of the Special Topic on Terahertz Frontiers: Quantum and Emergent Materials, Nanoscale Phenomena, Devices and Applications.

[a)]**Author to whom correspondence should be addressed:** msher@wesleyan.edu

ABSTRACT

This study presents a terahertz (THz) spectroscopy platform for the comprehensive characterization of charge carrier dynamics in photovoltaic (PV) materials. The system integrates steady-state conductivity measurements with electronically synchronized diode pump–THz probe measurements, enabling both equilibrium and non-equilibrium analyses of carrier behavior in silicon (Si) and germanium (Ge). In steady-state mode, frequency-dependent conductivity is extracted via Drude model analysis to obtain carrier scattering time and mobility. From the equilibrium carrier distribution, we determine an effective carrier lifetime that reflects the balance between the generation, diffusion, and recombination processes. The time-resolved component extends the measurements to the microsecond regime using pulsed diode laser excitation synchronized with the THz probe. This enables direct observation of carrier decay dynamics and reveals significantly longer lifetimes than those obtained from steady-state measurements, indicating fundamentally different physical processes governing each approach. Numerical simulations reconcile this discrepancy by capturing how spatial carrier distributions differ under steady-state and transient conditions. Under steady-state conditions, the effective lifetime is reduced due to constant carrier generation near the surface and continuous surface recombination. After pulsed-laser excitation, carrier diffusion toward the bulk reduces surface recombination and yields a longer transient lifetime. This shift in the spatial carrier distribution leads to differences in the observed lifetime and highlights the value of combined steady-state and time-resolved THz approaches for semiconductor characterization. The platform provides detailed insights into both microscopic transport properties and macroscopic carrier dynamics, supporting the optimized design of PV devices.

© 2026 Author(s). All article content, except where otherwise noted, is licensed under a Creative Commons Attribution (CC BY) license (https://creativecommons.org/licenses/by/4.0/). https://doi.org/10.1063/5.0311181

05 June 2026 18:55:54

I. INTRODUCTION

The growing global demand for energy and the urgent need to reduce greenhouse gas emissions have driven a worldwide transition toward renewable energy sources. Among these, photovoltaic (PV) stands out as a rapidly advancing technology. The sun delivers more energy to Earth in 1 h than humanity uses in an entire year, presenting a vast, underutilized resource.[1] Efficiently capturing this energy remains one of the most pressing scientific and engineering challenges. For solar PV, the ability to precisely measure and understand the behavior of charge carriers (electrons and holes) is central to materials development.

Carrier lifetime describes how long a photoexcited charge carrier remains mobile before recombining, while carrier mobility determines how fast it moves through the material under an electric field. Together, these properties govern the performance of nearly all semiconductor devices, from microprocessors and transistors to photodetectors, LEDs, and solar cells. Both lifetime and mobility affect the diffusion length, which is the average distance a carrier can travel before recombining and is a critical figure of merit for device efficiency. For many emerging materials to be used in PV devices, they must achieve diffusion lengths on the order of micrometers, which requires both long lifetimes (>10 ns) and high mobilities [$>10\,\mathrm{cm^2/(V\,s)}$].[2] Several emerging material systems have demonstrated exceptional promise in meeting these requirements. Metal halide perovskites have achieved certified efficiencies reaching 26.7% with carrier lifetimes exceeding $1\,\mu$s.[3–6] Carrier mobility as high as $400\,\mathrm{cm^2/(V\,s)}$ in MoS_2 and other two-

dimensional materials has shown great promise.[7,8] The high carrier mobility and microsecond carrier lifetime in silicon carbide and other wide-bandgap semiconductors are transforming power electronics.[9,10] Developments in single-crystal organic semiconductors have also surpassed the amorphous Si performance for flexible electronic applications.[11–13] A long diffusion length is essential for efficient charge collection in devices such as solar cells and requires both a long lifetime and high mobility.[14,15]

To understand what limits these properties, it is necessary to consider the physical processes governing recombination and transport. Longer lifetimes improve charge collection and are typically limited by nonradiative processes. Short lifetimes may reflect trap states in the bulk or at surfaces, while low mobility may result from poor crystallinity,[11–13] grain boundaries, or other scattering sources such as point defects and ionized impurities.[14] Accurate measurements of carrier lifetimes and mobilities are essential for guiding material synthesis, surface passivation, and device architecture.

Carrier lifetime measurement techniques fall into two main categories: contact-based and non-contact methods. Contact-based methods are sensitive to the full device structure, and the measured lifetimes may be influenced by junction quality, contact resistance, or parasitic capacitance rather than intrinsic material properties.[15] Non-contact techniques avoid the complications of making electrical connections, and different techniques are used to study carrier dynamics on different time scales. Quasi-steady-state photoconductance (QSSPC) and microwave-detected photoconductivity decay (μ-PCD) operate using microwave or radio frequencies and detect changes in conductance when light illuminates a material. These methods work well for measuring lifetimes from microseconds to milliseconds.[16,17] Time-resolved terahertz spectroscopy (TRTS) uses ultrafast optical pulses to generate and detect THz radiation and provides picosecond resolution for studying carrier dynamics.[18] At the purely optical end, time-resolved photoluminescence (TRPL) measures the light emitted by recombining carriers, offering a non-contact approach to estimate carrier lifetime.[15] Each technique presents distinct artifacts and limitations. Transient and steady-state measurements often yield different results because they probe distinct physical regimes,[19] and these methods do not distinguish between bulk and surface recombination. Reported lifetimes often differ by several orders of magnitude due to mismatched injection levels and varying time resolutions across techniques. The inherent limitations of the mechanical delay stages in conventional TRTS setups typically restrict the observation windows to the nanosecond scale. This is a significant drawback because TRTS can also simultaneously measure carrier mobility.[20,21]

Carrier mobility measurement has two categories: contact-based and contactless techniques. For contact-based techniques, the Hall effect measures mobility by applying a magnetic field and detecting the transverse voltage,[15] while FET methods extract it from current–voltage curves.[15,22] Non-contact techniques offer faster, non-destructive alternatives. TRTS and μ-PCD use a pump–probe setup where an optical pulse generates free carriers, and a THz or microwave pulse probes the induced conductivity, allowing mobility to be extracted directly without modeling assumptions.[17,23] Similar to lifetime measurements, each technique presents unique challenges. Contact-based measurements are often influenced by the metal electrodes that induce band bending, injection barriers, and interfacial effects.[24,25] Non-contact methods avoid these fabrication challenges but can produce inconsistent results across different measurement setups. Inter-laboratory studies confirm these discrepancies: Reported mobilities for identical samples have varied by more than 70% due to differences in calibration and data interpretation.[20] Mobility measurements from different techniques often disagree because they probe different length scales or operate under different injection regimes. This underscores the need for unified measurement approaches that distinguish bulk from interfacial transport and yield accurate, reproducible mobility values.

TRTS has emerged as a powerful non-contact technique for measuring both carrier lifetime and mobility. In optical-pump THz-probe experiments, the photoconductivity is extracted by monitoring the transmission of a single-cycle THz pulse through a photoexcited sample. In the time domain, excited charge carriers modify the amplitude and temporal shape of the transmitted THz electric field. By comparing the THz waveform transmitted through the sample with and without photoexcitation, the pump-induced change in the THz signal directly reflects the presence of photogenerated charge carriers.[21] The spectral information is obtained from Fourier transform of the time-domain signal, and the broad bandwidth of the THz probe enables direct access to the frequency-dependent conductivity, from which the carrier scattering time and mobility can be determined. Conventional TRTS studies already provide valuable insights and support material development, even though the probed time window is limited to only a few nanoseconds.[20,26,27]

To expand the capability of TRTS and probe slower dynamics, electronically synchronized pump–probe systems have been developed to overcome the temporal constraints of the mechanical delay lines. One system achieved tunable pump–probe delays from 600 ps to 200 μs by synchronizing a Q-switched laser with a THz emitter, enabling spatially resolved lifetime mapping in Si.[28] Another platform demonstrated digitally synchronized lasers and THz detection capable of sub-nanosecond resolution over time windows as long as 10 ms, enabling detailed studies of photoconductance decay in Si and Ge.[29] In metal halide perovskites, combining long- and short-delay TRTS measurements has revealed both ultrafast and long-lived recombination channels that are critical for optimizing tandem PV devices.[30] Despite this progress, a gap remains in fully linking the steady-state and transient carrier behaviors under realistic solar illumination. Many transient studies operate under high-injection conditions equivalent to tens to hundreds of Suns, which can introduce high-order recombination artifacts that mask the behavior relevant to the actual device performance.[3,15,16] Our work bridges this gap by operating near a 5-Sun equivalent intensity. This regime is ideal because it provides a strong experimental signal while suppressing overwhelming nonlinear effects, allowing us to probe carrier dynamics that are more representative of true 1-Sun operating conditions. To explicitly position this work within the landscape of existing characterization methods, Table I compares the key specifications and capabilities of our extended platform against conventional TRTS and other non-contact techniques.

In this study, we introduce a dual-mode THz platform that uses electronic synchronization between a diode pump laser and a THz probe to enable both steady-state and time-resolved

05 June 2026 18:55:54

© Author(s) 2026

TABLE I. Comparison of non-contact carrier lifetime measurement techniques. The table highlights the trade-offs between temporal resolution, measurement window, and access to frequency-dependent conductivity.

Technique	Probe type	Time resolution	Max window	Freq. resolved	Mobility	Steady state	Key limitations
TRTS (this work)	Broadband THz	5 μs	1 ms	Yes	Yes	Yes	Finite pump rise/fall time
Extended TRTS[28]	Broadband THz	600 ps	200 μs	Yes	Yes	No	High injection rate
Extended TRTS[29]	Broadband THz	200 ps	10 ms	Yes	Yes	No	High injection rate
Conventional fs-TRTS[26]	Broadband THz	1 ps	2 ns	Yes	Yes	No	High injection rate
μ-PCD[17]	Microwave	10 ns	ms	No	Yes	No	No spectral information
QSSPC[16]	Inductive RF coil	10–100 μs	CW	No	No	Yes	No transient dynamics
TRPL[15]	Optical	10–100 ps	1–10 μs	No	No	No	Radiative recombination only

measurements of carrier dynamics. For Si, in steady state, we measure a carrier lifetime of approximately 6 μs, while the transient lifetime extends to 34 μs. The observed difference arises from spatial dynamics: In the steady state, carriers accumulate near the surface, where recombination is faster, whereas in the transient case, diffusion into the bulk leads to a slower decay. Simulations based on the continuity equation validate this interpretation. We also apply the technique to Ge, confirming the broader utility of the system. This new platform, when combined with our previously demonstrated femtosecond-based TRTS system, enables continuous access to carrier dynamics from the picosecond to the microsecond time scale.[26] By bridging early-time and long-lived regimes, it offers a more complete picture of recombination and transport relevant to PV material design.

II. EXPERIMENTAL

TRTS is used to measure carrier dynamics in semiconductors over microsecond time scales. THz transmission experiments are performed on double-side polished n-type Si (1–5 Ω cm, 650 μm thick) and n-type Ge (1–3 Ω cm, 300 μm thick) wafers under ambient conditions without additional coatings. Figure 1 illustrates

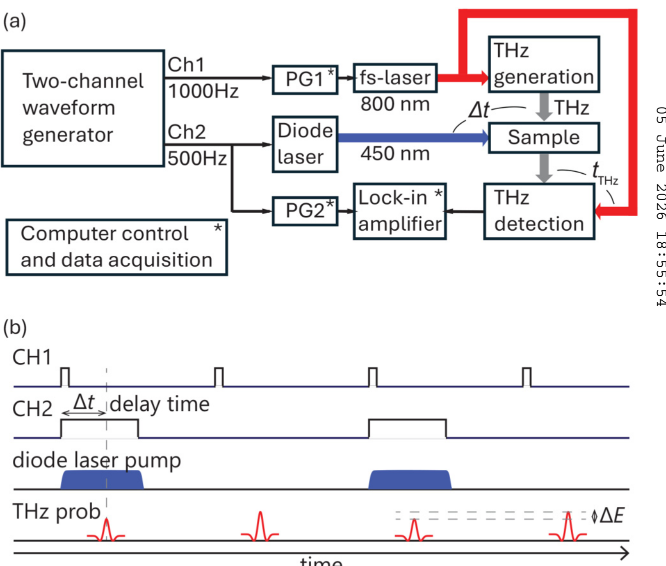

FIG. 1. (a) Schematic diagram of the electronically synchronized TRTS system. A two-channel waveform generator (CH1 at 1 kHz, CH2 at 500 Hz) controls two pulse generators (PG1 and PG2) that synchronize the femtosecond laser for THz generation/detection and the diode pump laser. THz pulses are generated and detected using an fs-laser, transmitted through the sample, and measured with a lock-in amplifier. The solid black lines correspond to electrical control signals, while the thick colored lines represent optical pulses. (b) Timing diagram showing the synchronization between CH1 and CH2, where each diode pulse coincides with every second THz probe pulse. The pump–probe delay Δt is computer-controlled to adjust the temporal offset between the diode pump and THz probe. Together, these panels illustrate both the optical–electronic configuration and the temporal synchronization enabling carrier-dynamics measurements over 0–800 μs.

05 June 2026 18:55:54

© Author(s) 2026

both the optical–electronic setup and the timing synchronization of the system. The two-channel waveform generator defines the experiment's primary clock signals: Channel 1 (CH1) at $f = 1$ kHz triggers a pulse generator (PG1) that synchronizes the femtosecond laser for THz generation and detection, while Channel 2 (CH2) at $f/2 = 500$ Hz drives the diode pump laser so that every second THz probe pulse coincides with a diode pulse. The output of CH2 also triggers a second pulse generator (PG2) connected to the lock-in amplifier for phase-locked detection of the pump modulation at frequency $f/2$. This detection scheme isolates the pump-induced change in the transmitted THz field by comparing alternating probe pulses, one with and one without optical excitation. An optical chopper, controlled by PG2, is used for baseline THz transmission measurements and removed during pump–probe acquisition. The pump–probe delay Δt is programmed electronically by adjusting the delay applied to PG1 through the computer interface, with the same delay signal sent to PG2 to maintain synchronization for detection.

THz probe pulses are generated using the two-color air-plasma method. A Ti:Sapphire laser amplifier provides 800 nm pulses with 2 mJ energy at a 1 kHz repetition rate. The output is divided into two optical paths: one for THz generation and the other for electro-optic detection. The 800 nm beam, combined with its second harmonic (400 nm), is focused into air to produce a coherent broadband THz pulse. At the sample position, the THz probe beam has an approximate diameter of 1 mm estimated from transmission through a pinhole. This pulse transmits through the sample and is detected via electro-optic sampling in a 1 mm ZnTe crystal. In the ZnTe crystal, the THz field induces a polarization rotation in a synchronized 800 nm gate beam, delayed by a mechanical delay stage by time t_{THz}, enabling sub-picosecond resolution of the THz electric field.[31,32]

For optical excitation, a 450-nm diode laser is modulated at 500 Hz with a 500 μs pulse duration (25% duty cycle). The beam is expanded 2.5× in both x and y using spherical lenses (40 and 100 mm focal lengths) and then compressed 2.5× along y using a cylindrical lens pair (100 and 40 mm). This produces an elliptical spot with $1/e$ diameters of approximately 2.1 mm (x) and 1.8 mm (y) on the sample, with 16 mW incident power at the surface. Both steady-state and transient measurements use identical 450 nm optical excitation with an intensity of 0.54 W/cm^2 (~5 Suns); only the timing protocol differs, with the pump–probe delay Δt scanned in transient mode and held fixed in steady-state operation.

In steady-state mode, first, the diode laser remains off while a mechanical chopper modulates the THz probe at 500 Hz, and the 800 nm gate beam records the baseline THz transmission $E_0(t_{\mathrm{THz}})$. Then, the diode laser is pulsed to generate photocarriers and the chopper is removed. Lock-in detection of the gate beam captures the differential waveform $\Delta E(t_{\mathrm{THz}}) = E_{\mathrm{pump}}(t_{\mathrm{THz}}) - E_0(t_{\mathrm{THz}})$, which corresponds to the change in THz transmission due to photocarrier generation [Fig. (1b)]. At a fixed pump–probe delay of $\Delta t = 275\,\mu$s, the carrier population reaches a quasi-steady state during the 500 μs excitation window.

In transient mode, the delay Δt_{pump} between the start of the diode pulse and the THz probe is scanned from 0 to 800 μs to resolve carrier dynamics. For each Δt_{pump}, the THz waveform is measured at its peak field amplitude t^*_{THz}, producing $\Delta E(\Delta t_{\mathrm{pump}}, t^*_{\mathrm{THz}})$, which traces the rise and decay of the carrier population. An exponential rise-and-decay model fits this curve to extract the effective carrier lifetime.

All measurements are performed at room temperature. The finite 5 μs rise and fall times of the diode laser are included in the fitting model. This electronically synchronized setup enables direct observation of microsecond-scale recombination dynamics.

III. RESULTS AND DISCUSSION

A. Steady-state measurement

THz transmission measurements are conducted on Si under optical excitation to examine the steady-state photocarrier dynamics (Fig. 2). The change in the THz signal, $\Delta E(t_{\mathrm{THz}})$, directly reflects the number of carriers generated by light exposure in the Si sample. Figure 2(a) displays two temporal waveforms: the transmitted THz electric field through unexcited Si, $E_0(t_{\mathrm{THz}})$, and the photoexcited differential THz electric field, $\Delta E(t_{\mathrm{THz}}) = E_{\mathrm{pump}}(t_{\mathrm{THz}}) - E_0(t_{\mathrm{THz}})$, induced by the optical pump. For clarity, $E_0(t_{\mathrm{THz}})$ is scaled by a factor of 0.1 and represents the baseline transmission through the Si sample without optical excitation. Figure 2(b) presents the peak value of $E_0(t^*_{\mathrm{THz}})$ and its corresponding $\Delta E(t^*_{\mathrm{THz}})$, based on 100 repeated measurements. The actual peak electric field of $E_0(t^*_{\mathrm{THz}})$, without scaling, is $242 \pm 1\,\mu$V, which serves as the baseline transmission through unexcited Si. The reported signal, measured in μV, reflects the signal detected by the lock-in amplifier and is proportional to the THz electric field strength.[31]

The average differential electric field $\Delta E = -9.9 \pm 0.2\,\mu$V indicates a reduction in THz transmission due to the interaction with photogenerated carriers. The peak ratio $\Delta E/E_0 \approx -0.041$ corresponds to a 4.1% reduction in THz transmission caused by the presence of steady-state carriers. The steady-state photoconductivity σ is calculated using the following relation:[20]

$$\sigma = \left(\frac{1+N}{Z_0 d}\right)\left(\frac{-\Delta E}{E_0}\right), \tag{1}$$

where $N = 3.41$ is the refractive index of Si, $Z_0 = 377\,\Omega$ is the impedance of free space, and $d = 394$ nm is the depth of the photoexcited region. Substituting the given values yields a photoconductivity of approximately 12 S/cm due to photocarrier generation.

Following the time-domain measurements, the data are Fourier-transformed to obtain spectral information across the 0–3 THz range, enabling the analysis of the frequency-dependent photocarrier response. Figure 3(a) compares the amplitude of the transmitted THz field through unexcited Si, $E_0(\omega)$, and the photo-induced differential field, $\Delta E(\omega)$. The presence of photocarriers leads to clear attenuation patterns, illustrating how optical excitation modifies the THz transmission across different frequencies. Figure 3(b) presents the complex conductivity $\sigma(\omega)$, calculated from Eq. (2), where $-\Delta E(\omega)/E_0(\omega)$ is directly proportional to $\sigma(\omega)$.

To connect these spectral changes with the carrier transport properties, the complex conductivity $\sigma(\omega)$ is modeled. A widely used approach is the Drude model, which describes free-carrier transport and relates the conductivity to the scattering time τ_{sc},

$$\sigma(\omega) = \frac{\sigma_{\mathrm{dc}}}{1 - i\omega\tau_{\mathrm{sc}}}, \tag{2}$$

05 June 2026 18:55:54

© Author(s) 2026

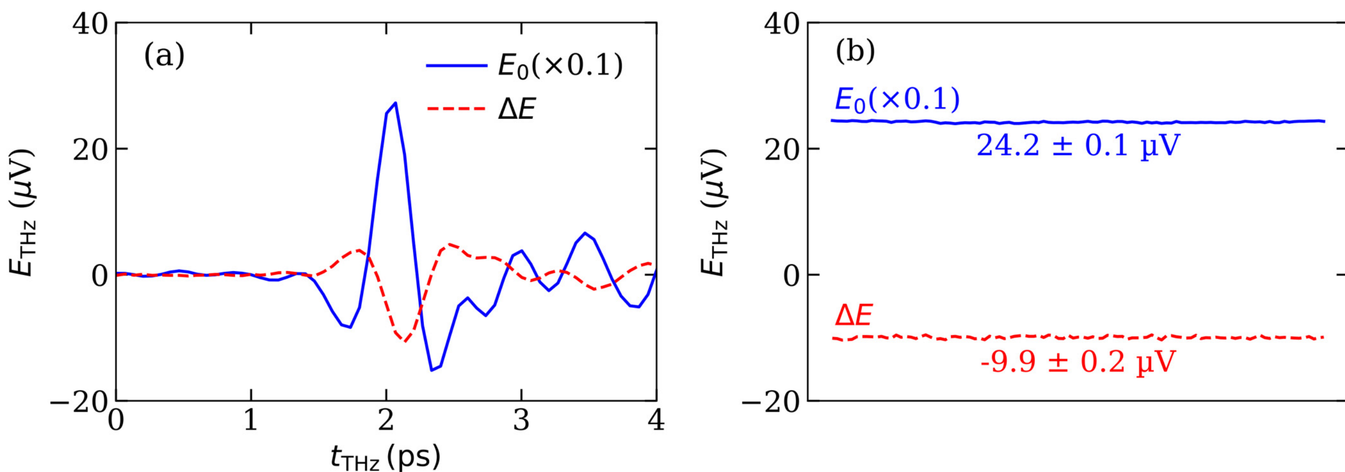

FIG. 2. THz transmission measurements through a Si sample. (a) Temporal waveforms of the undisturbed THz electric field, $E_0(t_{THz})$, transmitted through Si without optical excitation (blue solid line). Differential THz electric field, $\Delta E(t_{THz})$, measured under photoexcitation of the Si sample (red dashed line). For clarity, $E_0(t_{THz})$ is scaled by a factor of 0.1. (b) Peak value of $E_0(t^*_{THz})(\times 0.1)$ and its corresponding $\Delta E(t^*_{THz})$ are averaged from 100 repeated measurements, yielding 24.2 ± 0.1 and $-9.9 \pm 0.2\,\mu$V, respectively, illustrating the change in THz transmission induced by the photoexcitation. The reported signal, measured in μV, reflects the signal detected by the lock-in amplifier and is proportional to the THz electric field strength.

where σ_{dc} is the DC conductivity. The real part indicates energy dissipation due to carrier motion, while the imaginary part is related to the phase shift of the THz field. We find that the Drude model effectively captures transport in our samples, which are crystalline semiconductors. Alternative models, such as the Drude–Smith or localization frameworks, can be employed when carrier backscattering, disorder, or localization effects are significant.[18,20] The solid lines represent the Drude model fits, which allow for the determination of key transport parameters σ_{dc} and τ_{sc}, and from these parameters, the carrier mobility μ can be calculated as $\mu = q\tau_{sc}/m^*$, where q is the elementary charge and m^* is the effective mass of the charge carrier.

The Drude model fit in Fig. 3(b) yields key transport parameters: a DC conductivity of $\sigma_{dc} = 15 \pm 1$ S/cm and a carrier scattering time of $\tau_{sc} = 120 \pm 5$ fs, corresponding to a mobility of $\mu = 800 \pm 30\,\text{cm}^2/(\text{V s})$. These values align with known Si properties and validate the use of THz spectroscopy for transport analysis.[33,34] For Ge, mobility is presented in Fig. S1 in the

05 June 2026 18:55:54

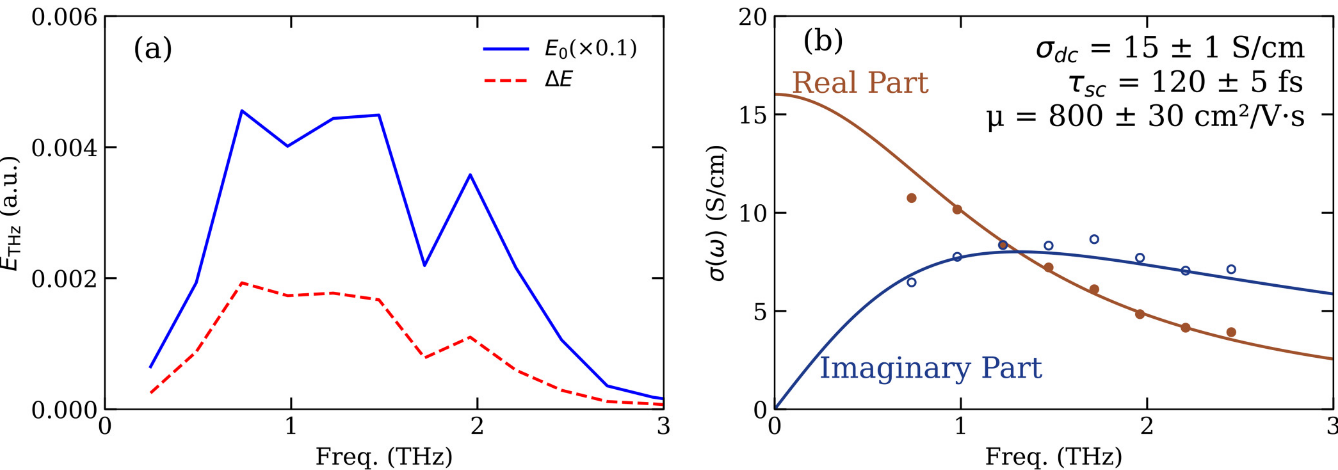

FIG. 3. Frequency-domain analysis of THz transmission through Si. (a) The spectral components of THz pulses from 0 to 3 THz, comparing the unexcited reference field $E_0(\omega)$ (scaled by 0.1, solid blue line) and the photoinduced differential field $\Delta E(\omega)$ (red dashed line). (b) Frequency-dependent conductivity $\sigma(\omega)$ for the real (brown filled circles) and imaginary (dark-blue open circles) components, along with Drude model fits (solid lines). The fit yields a DC conductivity $\sigma_{dc} = 15 \pm 1$ S/cm, a carrier scattering time $\tau_{sc} = 120 \pm 5$ fs, and the extracted parameters give a mobility of $\mu = 800 \pm 30\,\text{cm}^2/(\text{V s})$.

© Author(s) 2026

supplementary material, with the mobility estimated to be approximately $4500 \pm 300\,\text{cm}^2/\text{V s}$, which is consistent with the typical values for intrinsic Ge at room temperature.[33]

To extract the steady-state carrier lifetime from THz measurements, we relate the measured THz transmission change to the steady-state photoconductivity. The surface reflectivity R is treated as an optical loss in this measurement. The absorbed fraction of the incident power is $(1 - R)$, leading to a carrier generation rate $G = \frac{P(1-R)}{h\nu V}$, where P is the incident optical power, $h\nu$ is the photon energy, and V is the illuminated sample volume (beam area A times depth of the photoexcited region d). In steady state, G is balanced by recombination, which is the carrier density n divided by the carrier lifetime τ, leading to a constant carrier density of $n = G\tau$. This photogenerated carrier population determines the material's photoconductivity, σ [Eq. (3)], which relates to n and μ by $\sigma = nq\mu$, where q is the elementary charge. Substituting these expressions yields the carrier lifetime as

$$\tau = \frac{h\nu A}{P(1-R)} \cdot \frac{1+N}{Z_0 \mu q} \cdot \frac{-\Delta E}{E_0}. \tag{3}$$

Using the experimental parameters: $P = 16 \pm 2\,\text{mW}$, $\mu = 800 \pm 30\,\text{cm}^2/(\text{V s})$, pump beam area $A = 0.0290 \pm 0.0029\,\text{cm}^2$, $-\Delta E/E_0 = 0.040 \pm 0.002$, and $R = 0.40$, the steady-state carrier lifetime in Si is calculated to be $\tau = 6 \pm 2\,\mu\text{s}$. A similar calculation was performed for Ge using $R = 0.40$ and mobility $\mu = 4500 \pm 300\,\text{cm}^2/(\text{V s})$. This yielded a calculated steady-state carrier lifetime in Ge of $\tau = 2.5 \pm 0.5\,\mu\text{s}$.

The steady-state lifetime calculation does not include spatial effects such as carrier diffusion out of the THz probe area. In our sample, the diffusion length estimated from the mobility and lifetime suggests that lateral diffusion is negligible.[29] The spatial overlap between the optical pump and the THz probe is also neglected, and including the spatial effects could further improve the accuracy of the extracted lifetime.[35] Steady-state measurements remain useful for evaluating carrier behavior when generation and recombination are balanced. To directly observe the recombination dynamics without steady-state conditions, we turn to time-resolved THz measurements using pulsed excitation. This approach captures the carrier decay after the pump pulse and enables extraction of the transient carrier lifetime.

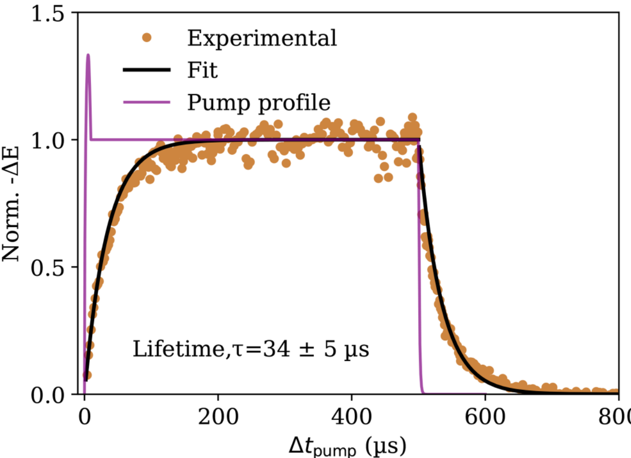

FIG. 4. Diode pump and THz probe transient measurement with corresponding pump profile. The normalized differential transmission ($-\Delta E$) is plotted as a function of time, showing the rise, steady-state plateau, and decay of photocarriers. The temporal evaluation of experimental data (orange circles) is fitted with a model (black curve), yielding a carrier lifetime of $\tau = 34 \pm 5\,\mu\text{s}$. The magenta curve shows the normalized pump intensity profile during the $500\,\mu\text{s}$ excitation pulse.

B. Transient measurement

Figure 4 presents the time-resolved differential THz transmission signal in Si following pulsed optical excitation. This measurement captures the full carrier dynamics, including the accumulation of photocarriers that leads to a steady-state population during the laser pulse, and their decay after the excitation ends. The change in THz transmission, $\Delta E(\Delta t_{\text{pump}}, t^*_{\text{THz}})$, reflects the evolving carrier population, as free carriers interact with and attenuate the transmitted THz field. Electronic synchronization between the diode laser pump and the THz probe allows for time-resolved measurements over hundreds of microseconds, enabling direct access to slow recombination processes.

The carrier response is modeled using a piecewise exponential function,

$$\Delta E(\Delta t_{\text{pump}}, t^*_{\text{THz}}) = \begin{cases} \Delta E_0 \left(1 - e^{-\Delta t_{\text{pump}}/\tau}\right), & 0 \le \Delta t_{\text{pump}} < t_{\text{pulse}} \\ \Delta E_0\, e^{-(\Delta t_{\text{pump}} - t_{\text{pulse}})/\tau}, & \Delta t_{\text{pump}} \ge t_{\text{pulse}}. \end{cases} \tag{4}$$

Here, ΔE_0 is the steady-state value of the THz transmission change during the illumination. We fit the normalized data with τ as a single free parameter. The first segment of the model describes the exponential rise in carrier density during illumination, where generation competes with recombination. The second segment captures the decay of the carrier population after the pump is turned off, reflecting intrinsic recombination in the absence of continued generation.

Fitting this model to the normalized experimental data yields a transient carrier lifetime of $\tau = 34 \pm 5\,\mu\text{s}$ for Si. The consistency of the fit across both the rising and falling segments indicates that a single recombination process governs the dynamics. A similar fit is applied to the normalized transient decay data for Ge, as shown in Fig. S1 in the supplementary material, yielding a transient carrier lifetime of $\tau = 8 \pm 5\,\mu\text{s}$.

The magenta curve in Fig. 4 shows the normalized intensity profile of the diode laser used for optical excitation. The laser is programmed to deliver a $500\,\mu\text{s}$ rectangular pulse. We observe the actual rise and fall times of $5\,\mu\text{s}$ with an initial transient at the onset of the pump pulse, where the measured intensity briefly overshoots before settling at a steady-state level. This introduces minor uncertainty in the precise timing of the carrier dynamics. The $5\,\mu\text{s}$ rise and fall times are included as error bars in the transient measurement.

Notably, the fitted transient lifetime ($34 \pm 5\,\mu\text{s}$) is significantly longer than the steady-state lifetime ($6 \pm 2\,\mu\text{s}$) for Si. A similar discrepancy is observed for Ge, where the transient lifetime

05 June 2026 18:55:54

© Author(s) 2026

($8 \pm 5\,\mu$s) exceeds the steady-state estimated lifetime of $\tau = 2.5 \pm 0.5\,\mu$s (Fig. S1 in the supplementary material). This discrepancy reflects the fundamental differences in the measurement conditions. Steady-state measurements involve a dynamic balance between generation, recombination, and diffusion, whereas transient measurements probe carrier decay directly after excitation ceases, with recombination and diffusion governing the carrier distribution profile as a function of time. Since recombination depends on both surface and bulk traps, the evolving carrier distribution strongly influences the measured lifetime. Reconciling these differences is essential for the accurate characterization of carrier lifetimes and for optimizing Si-based optoelectronic devices.

C. Simulation

We use a 1D time-dependent diffusion–recombination model to simulate carrier dynamics in Si under pulsed optical excitation. In this simulation, the surface recombination and bulk lifetime are adjustable parameters used to match the experimental data. The governing equation is as follows:

$$\frac{\partial n(x,t)}{\partial t} = D\frac{\partial^2 n(x,t)}{\partial x^2} - \frac{n(x,t)}{\tau} + G(x,t). \tag{5}$$

For generalization, Δt_{pump} is replaced with t in Eq. (5). Here, $n(x, t)$ is the photogenerated carrier concentration at depth x and time t. The diffusion coefficient D is assumed to be constant, and in this one-dimensional model, outward diffusion in the lateral directions is ignored. The mobility–diffusivity relation is given by the Einstein relation, $D = \mu \frac{k_B T}{q}$, where μ is taken from the aforementioned Drude model fit, k_B is the Boltzmann constant, and $T = 300$ K is the ambient temperature. The bulk carrier lifetime τ is varied to match the experimental decay dynamics.

The generation rate $G(x, t)$ captures both the spatial carrier generation profile and the temporal shape of the pump pulse, expressed as $G(x,t) = G_0\, e^{-\alpha x} \cdot f(t)$. Here, $G_0 = 2.1 \times 10^{22}\,\text{cm}^{-3}\,\text{s}^{-1}$ is the peak generation rate with reflectivity taken into account. The spatial carrier generation profile is determined by the absorption coefficient $\alpha = 2.54 \times 10^4\,\text{cm}^{-1}$. The function $f(t)$ represents the normalized temporal profile of the optical pulse, modeled using a piecewise exponential function similar to the form of Eq. (4), with rise and fall time constants of $5\,\mu$s and a pulse duration of $500\,\mu$s.

Surface recombination is modeled at both the front ($x = 0$) and back ($x = L$) surfaces of the domain using Robin boundary conditions, which relate the diffusive flux to the carrier concentration via surface recombination velocities. At the front surface ($x = 0$),

$$D\frac{\partial n}{\partial x}\bigg|_{x=0} = S_{\text{front}}\, n(0,t), \tag{6}$$

where S_{front} is the front surface recombination velocity. At the back surface ($x = L$),

$$-D\frac{\partial n}{\partial x}\bigg|_{x=L} = S_{\text{back}}\, n(L,t), \tag{7}$$

where S_{back} is the back surface recombination velocity, and $L = 650\,\mu$m is the thickness of the wafer. These conditions account for carrier losses at the surfaces, with the flux direction adjusted according to the outward normal at each boundary. Since there are no asymmetric surface treatments, we assume $S_{\text{front}} = S_{\text{back}}$ for simplicity.

A non-uniform spatial grid resolves steep near-surface gradients in the simulation. The grid spacing ranges from 1 nm near the boundaries to 50 nm in the interior. The initial carrier concentration is set to $n(x, 0) = 0$ across the domain. The temporal evolution is computed using a fixed time step of $0.005\,\mu$s over a total duration of $800\,\mu$s.

To solve Eq. (5) numerically, we use a fully implicit finite-difference scheme.[36] The time derivative is discretized using the backward Euler method, and the spatial second derivative is approximated using second-order finite differences adapted for non-uniform grid spacing. We solve the time-dependent diffusion–recombination equation at each time step by advancing the solution using

$$\mathbf{A} \cdot \mathbf{n}^{k+1} = \mathbf{d}^{k+1}. \tag{8}$$

Here, $\mathbf{n}^{k+1}$ is the column vector of carrier concentrations at all spatial positions at time step $k + 1$, and $\mathbf{d}^{k+1}$ is the right-hand side vector containing known terms from time step k. The tridiagonal matrix $\mathbf{A}$ is constructed such that each row j contains the finite-difference coefficients related to each spatial position node, a_j, b_j, and c_j. Specifically, for each spatial node j, the jth row of the matrix equation expands to the scalar form,

$$a_j n_{j-1}^{k+1} + b_j n_j^{k+1} + c_j n_{j+1}^{k+1} = d_j^{k+1}. \tag{9}$$

The tridiagonal structure of $\mathbf{A}$ arises naturally from the nearest-neighbor coupling in the finite-difference scheme, where a_j represents the coefficient of the left neighbor (n_{j-1}), b_j is the diagonal coefficient for the current node (n_j), and c_j is the coefficient of the right neighbor (n_{j+1}). These position-dependent coefficients incorporate the effects of diffusion, bulk recombination, and surface recombination terms, while d_j^{k+1} contains the known concentration from the previous time step k and the generation term.

The linear system at each interior node ($j = 2$ to $N - 1$) takes the form shown above, where the tridiagonal coefficients are

$$\begin{aligned} a_j &= -\frac{2\Delta t D}{(\Delta x_j + \Delta x_{j-1})\Delta x_{j-1}}, \\ c_j &= -\frac{2\Delta t D}{(\Delta x_j + \Delta x_{j-1})\Delta x_j}, \\ b_j &= 1 - (a_j + c_j) + \frac{\Delta t}{\tau}, \\ d_j^{k+1} &= n_j^k + \Delta t\, G_j^{k+1}, \end{aligned} \tag{10}$$

where $\Delta x_j = x_{j+1} - x_j$ and $\Delta x_{j-1} = x_j - x_{j-1}$. The surface recombination terms are included only near the boundaries through spatial masks.

05 June 2026 18:55:54

© Author(s) 2026

Near the boundaries, the coefficients are adjusted to enforce the Robin boundary conditions. At the front surface ($j = 1$),

$$\begin{aligned} a_1 &= 0, \\ c_1 &= -\frac{2D\Delta t}{\Delta x_1^2}, \\ b_1 &= 1 - c_1 + \frac{\Delta t}{\tau} + \frac{2S_{\text{front}}\Delta t}{\Delta x_1}, \\ d_1 &= n_1^k + \Delta t \cdot G_1^{k+1}. \end{aligned} \tag{11}$$

At the back surface ($j = N$),

$$\begin{aligned} a_N &= -\frac{2D\Delta t}{\Delta x_{N-1}^2}, \\ c_N &= 0, \\ b_N &= 1 - a_N + \frac{\Delta t}{\tau} + \frac{2S_{\text{back}}\Delta t}{\Delta x_{N-1}}, \\ d_N &= n_N^k + \Delta t \cdot G_N^{k+1}. \end{aligned} \tag{12}$$

These adjustments enforce the diffusive flux–carrier density balance required at the surfaces through Robin boundary conditions.

The resulting system is solved at each time step using the Thomas algorithm.[36] This algorithm performs a forward elimination step that transforms $\mathbf{A}$ into upper-triangular form, followed by a backward substitution step to solve for $\mathbf{n}^{k+1}$. The overall computational cost per time step is $O(N)$, where N is the number of grid points. This approach is well-suited for non-uniform grids and ensures numerical stability, even in the presence of sharp carrier gradients and fast recombination near surfaces.

To identify the best-fit physical parameters, we systematically sweep the bulk lifetime τ from 50 to 900 μs and the surface recombination velocity S from 1000 to 10 000 cm/s (Figs. S2 and S3 and Table S1 in the supplementary material). The simulated carrier concentration dynamics are compared with the experimental THz decay curves, and the optimal parameter set is selected based on agreement with both the rise and decay of the signal. For Si, the best agreement with the experimental data is achieved with a bulk lifetime exceeding 300 μs and a surface recombination velocity of 4000 $\pm$ 200 cm/s applied symmetrically at both the front and back surfaces. For Ge, the best agreement with the experimental data is obtained with a bulk $\tau = 10 \pm 4\,\mu$s and $S = 4480 \pm 50$ cm/s, as shown in Figs. S1 and S4 in the supplementary material. Any deviation from these values for either τ or S results in a noticeable mismatch with the measured values for Ge.

Figure 5 illustrates the carrier dynamics in Si during a 500 μs pulsed excitation, using experimental data and simulations to reveal how the carrier concentration evolves temporally and spatially. Figure 5(a) shows the temporal evolution of the carrier concentration, comparing experimental measurements with simulation predictions, while Fig. 5(b) illustrates the spatial distribution of carriers at specific time points during and after the pulse. Simulations are essential in this analysis because they model key processes, such as carrier generation, diffusion, and recombination, which cannot be directly observed experimentally. By providing a detailed picture of how carriers behave spatially, the simulations explain the key differences. We find that the shorter steady-state lifetime dominated by surface recombination vs the longer transient lifetime governed by slower bulk recombination, offering critical insights into the underlying dynamics.

Figure 5(b) shows that during the first few microseconds of illumination, carriers are generated primarily near the Si surface due to the exponential absorption profile of the pump light, $G(x) \propto e^{-\alpha x}$. The distribution at 1 μs shows a sharp decay into the bulk, forming a steep surface-weighted profile. By 5 μs, some carrier diffusion toward the bulk becomes visible, but the profile remains heavily skewed toward the surface. As illumination continues, diffusion becomes more prominent. At 10 μs, the profile extends further into the bulk, showing a gentler slope than at earlier times. The surface concentration stays high due to continuous generation, while the bulk gradually fills with carriers. At 200 μs, the distribution stretches across the entire sample width, approaching a linear gradient.

At 200 μs, the system is in a steady state. From 200 to 500 μs, the carrier distribution remains unchanged, showing that carrier generation, diffusion, and recombination are in dynamic balance. The profile maintains a surface-weighted shape, gradually decreasing from the illuminated front side to the back side of the sample. In this steady state, the recombination mechanism is dominated by the surface. Although carriers are continuously generated near the surface, they recombine quickly due to the high surface recombination velocity.

Immediately after the excitation turns off at 500 μs, the carrier distribution changes sharply. Surface recombination causes a rapid decrease in the carrier density near the surface. At 501 μs, the maximum peak of the carrier distribution shifts deeper into the bulk, and the surface concentration decreases visibly. At 505 μs, the carrier distribution maximum begins to shift to 150 μm from the surface, and its amplitude decreases to 70% of its value at turn-off. The carrier concentration at the surface also reduces further, forming a more pronounced bell-shaped distribution.

05 June 2026 18:55:54

D. Discussion

In Si, a clear discrepancy is observed between the steady-state and transient lifetimes, which stems from the distinct carrier distributions in each condition. The steady-state lifetime is measured to be 6 $\pm$ 2 μs, whereas the transient lifetime extends to 34 $\pm$ 5 μs. In the steady-state regime, continuous generation leads to carrier distribution in a surface-weighted profile, in which carrier density is higher near the surfaces. Because surface recombination is very strong in this region, the effective lifetime is drastically shortened. In contrast, in the transient regime, once the pump pulse ceases, carriers near the surface recombine rapidly, but a fraction of carriers persists in the surface region and continues to contribute to the measured signal. As a result, the transient lifetime appears longer than the steady-state lifetime but still does not represent the intrinsic bulk alone. This strong coupling between the surface and bulk effects also explains the uncertainty in extracting the true bulk lifetime of Si from the fits. A wide range of (τ, S) combinations can

© Author(s) 2026

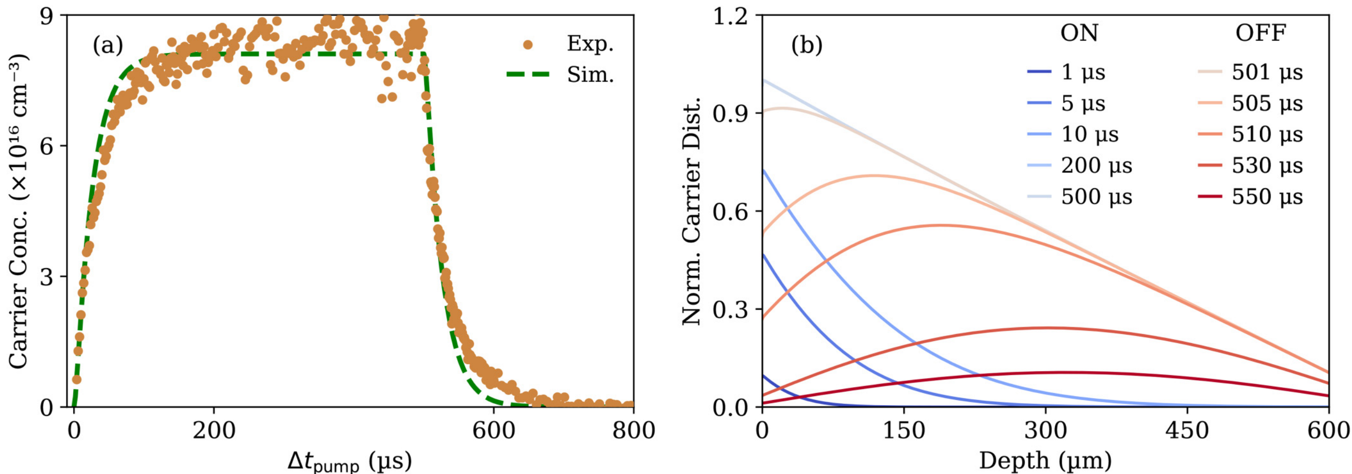

FIG. 5. Numerical simulation of carrier dynamics in Si under a 500 μs optical pulse. (a) Temporal evolution of carrier concentration comparing experimental data (orange circles) with simulation results (green dashed line). (b) Spatial carrier distribution at selected times during and after the pulse, illustrating surface-weighted steady-state profiles and the transition to bulk-dominated decay. The simulation shown here uses a bulk lifetime of $\tau \approx 300\,\mu$s and a surface recombination velocity of $S \approx 4000$ cm/s applied symmetrically at both surfaces.

reproduce the data, and the simulations indicate that the bulk lifetime exceeds 300 μs, without a unique value (Fig. S2 in the supplementary material).

In Ge, a material known for shorter lifetime and high carrier mobility makes it an ideal material for demonstrating the strength of our model. The experimentally measured transient lifetime is $8 \pm 5\,\mu$s, which is essentially the same as the bulk lifetime (10 μs) used in the simulation. After the pump pulse ends, the high mobility of carriers in Ge allows them to move rapidly into the bulk, reducing the role of surface recombination and leaving the decay governed almost entirely by the bulk processes. As a result, the simulation closely matches the experimental response, capturing both the carrier buildup during excitation and the decay after the pump with minimal uncertainty. This close agreement between transient and bulk lifetimes in Ge highlights the ability of our model to capture intrinsic material properties in systems where the combination of high mobility and relatively short bulk lifetime suppresses surface effects and makes the modeling more effective.

Our studies on Si and on Ge illustrate how the model reconciles steady-state and transient measurements by explicitly accounting for spatial carrier distributions. In steady-state, carriers remain concentrated near the surface, where recombination dominates and yields a short effective lifetime. In the transient regime, surface carriers are rapidly depleted after the pump pulse, leaving a distribution that decays more slowly under bulk control. For Si, the competing influence of bulk and surface recombination creates ambiguity and prevents a clear determination of the bulk lifetime. For Ge, the combination of a shorter bulk lifetime and higher mobility reduces the impact of surface recombination, leading to a close agreement between the transient and bulk lifetimes. These results reveal the physical origin of discrepancies between steady-state and transient measurements and demonstrate the model's ability to capture carrier dynamics across materials.

Future work could employ two-color excitation to reduce uncertainties in bulk-lifetime extraction. The current experiments use only 450 nm light, which is strongly absorbed near the Si surface and leads to surface-weighted carrier distribution. By incorporating longer-wavelength excitation that penetrates deeper into the bulk, it will be possible to systematically vary the initial carrier profile and better separate the effects of surface and bulk recombination. In addition, extending these measurements to surface-passivated samples would provide an independent mean of suppressing surface recombination and validating the bulk-dominated dynamics. This approach would yield more accurate bulk lifetime measurements with reduced surface influence, improving the characterization of semiconductor materials for solar cells and electronic devices.

05 June 2026 18:55:54

IV. CONCLUSION

In conclusion, this study successfully demonstrates an extended TRTS platform designed specifically for accurately measuring microsecond-scale carrier lifetimes in PV materials under illumination conditions closer to 1-Sun intensity. By combining steady-state photoconductivity analysis with electronically synchronized diode pump–THz probe transient measurements, this system provides detailed insights into carrier dynamics.

In our study, using a 450 nm diode laser excitation on Si and Ge wafers, we found the carrier mobilities to be $800 \pm 30\,\mathrm{cm^2/(V\,s)}$ for Si and $4500 \pm 300\,\mathrm{cm^2/V\,s}$ for Ge. For Si, the measured steady-state and transient lifetimes were 6 ± 2 and $34 \pm 5\,\mu$s, respectively. The simulation indicated that these are strongly influenced by surface recombination, and the simulated surface recombination velocity was 4000 ± 200 cm/s with bulk carrier lifetime exceeding 300 μs. In contrast, for Ge, the measured steady-state and transient lifetimes were $2.5 \pm 0.5\,\mu$s and $8 \pm 5\,\mu$s, respectively. Our simulation found that a bulk lifetime of $10 \pm 4\,\mu$s and a surface recombination

© Author(s) 2026

velocity of 4480 ± 50 cm/s best matched the combined transient and steady-state data. In Ge, due to higher carrier mobility and shorter bulk lifetime, the transient measurement mostly reflected the bulk property.

By combining steady-state and transient THz measurements with numerical modeling, we obtained a comprehensive understanding of carrier transport and recombination dynamics. Steady-state frequency-domain analysis using the Drude model provided key transport parameters, including DC conductivity and mobility, describing equilibrium carrier behavior. The comparison between steady-state and transient measurements revealed different effective lifetimes, with the steady-state lifetime being shorter due to enhanced surface recombination under continuous illumination. Both surface and bulk recombination contribute to these lifetimes, and their combined effects can be simulated in detail to reproduce the transient response, linking carrier generation, diffusion, and recombination across surface and bulk regions. Together, these results establish the extended TRTS platform as a unified framework for probing and optimizing carrier dynamics in optoelectronic materials.

SUPPLEMENTARY MATERIAL

See the supplementary material for microsecond carrier lifetime measurements for germanium and simulation curves with a wide parameter sweep for both silicon and germanium.

ACKNOWLEDGMENTS

The authors would like to acknowledge the National Science Foundation (NSF) DMR-2316827 for funding.

AUTHOR DECLARATIONS

Conflict of Interest

The authors have no conflicts to disclose.

Author Contributions

K. M. Ashikur Rahman: Formal analysis (lead); Investigation (lead); Methodology (equal); Visualization (lead); Writing – original draft (lead); Writing – review & editing (equal). **Bin Yun:** Formal analysis (supporting); Investigation (supporting); Methodology (supporting); Writing – review & editing (supporting). **Jack L. Root:** Formal analysis (supporting); Investigation (supporting); Methodology (equal); Writing – review & editing (supporting). **George A. Blinick:** Investigation (supporting); Methodology (supporting). **Meng-Ju Sher:** Conceptualization (lead); Supervision (lead); Visualization (supporting); Writing – review & editing (lead).

DATA AVAILABILITY

The data that support the findings of this study are available from the corresponding author upon reasonable request.

REFERENCES

[1] L. Hammarström, "Overview: Capturing the sun for energy production," Ambio **41**(Suppl 2), 103–107 (2012).

[2] R. Jaramillo, M.-J. Sher, B. K. Ofori-Okai, V. Steinmann, C. Yang, K. Hartman, K. A. Nelson, A. M. Lindenberg, R. G. Gordon, and T. Buonassisi, "Transient terahertz photoconductivity measurements of minority-carrier lifetime in tin sulfide thin films: Advanced metrology for an early stage photovoltaic material," J. Appl. Phys. **119**(3), 035101 (2016).

[3] M. A. Green, E. D. Dunlop, M. Yoshita, N. Kopidakis, K. Bothe, G. Siefer, D. Hinken, M. Rauer, J. Hohl-Ebinger, and X. Hao, "Solar cell efficiency tables (version 64)," Progr. Photovoltaics Res. Appl. **32**(7), 425–441 (2024).

[4] C. Yang, W. Hu, J. Liu, C. Han, Q. Gao, A. Mei, Y. Zhou, F. Guo, and H. Han, "Achievements, challenges, and future prospects for industrialization of perovskite solar cells," Light Sci. Appl. **13**(1), 227 (2024).

[5] D. Kiermasch, P. Rieder, K. Tvingstedt, A. Baumann, and V. Dyakonov, "Improved charge carrier lifetime in planar perovskite solar cells by bromine doping," Sci. Rep. **6**, 39333 (2016).

[6] S. D. Stranks, G. E. Eperon, G. Grancini, C. Menelaou, M. J. P. Alcocer, T. Leijtens, L. M. Herz, A. Petrozza, and H. J. Snaith, "Electron-hole diffusion lengths exceeding 1 micrometer in an organometal trihalide perovskite absorber," Science **342**(6156), 341–344 (2013).

[7] J. Hong, Z. Hu, M. Probert, K. Li, D. Lv, X. Yang, L. Gu, N. Mao, Q. Feng, L. Xie *et al.*, "Exploring atomic defects in molybdenum disulphide monolayers," Nat. Commun. **6**, 6293 (2015).

[8] H. Fang, S. Chuang, T. C. Chang, K. Takei, T. Takahashi, and A. Javey, "High-performance single layered wse_2 p-fets with chemically doped contacts," Nano Lett. **12**(7), 3788–3792 (2012).

[9] T. Kimoto, "Material science and device physics in SiC technology for high-voltage power devices," Jpn. J. Appl. Phys. **54**(4), 040103 (2015).

[10] G. Gupta and E. Ahmadi, "(Ultra)wide-bandgap semiconductors for electric vehicles," MRS Bull. **49**(7), 730–737 (2024).

[11] J. Liu, H. Zhang, H. Dong, L. Meng, L. Jiang, L. Jiang, Y. Wang, J. Yu, Y. Sun, W. Hu *et al.*, "High mobility emissive organic semiconductor," Nat. Commun. **6**(1), 10032 (2015).

[12] Z. He, K. Asare-Yeboah, and S. Bi, "Advances in charge carrier mobility of diketopyrrolopyrrole-based organic semiconductors," Coatings **14**(9), 1080 (2024).

[13] Z. Wang, X. Wu, S. Zhang, S. Yang, P. Gao, P. Huang, Y. Xiao, X. Shen, X. Yao, D. Zeng *et al.*, "Breaking the mobility–stability dichotomy in organic semiconductors through adaptive surface doping," Proc. Natl. Acad. Sci. U.S.A. **122**(14), e2419673122 (2025).

[14] S. M. Sze, *Semiconductor Devices: Physics and Technology* (John Wiley & Sons, 2008).

[15] D. K. Schroder, *Semiconductor Material and Device Characterization*, 3rd ed. (Wiley-Interscience, Hoboken, NJ, 2006).

[16] A. Ronald, "Sinton and andres cuevas. Contactless determination of current–voltage characteristics and minority-carrier lifetimes in semiconductors from quasi-steady-state photoconductance data," Appl. Phys. Lett. **69**(17), 2510–2512 (1996).

[17] T. Asada, Y. Ichikawa, and M. Kato, "Carrier lifetime measurements in semiconductors through the microwave photoconductivity decay method," J. Visual. Exp. **146**, e59007 (2019).

[18] R. Ulbricht, E. Hendry, J. Shan, T. F. Heinz, and M. Bonn, "Carrier dynamics in semiconductors studied with time-resolved terahertz spectroscopy," Rev. Mod. Phys. **83**(2), 543–586 (2011).

[19] R. K. Ahrenkiel, N. Call, S. W. Johnston, and W. K. Metzger, "Comparison of techniques for measuring carrier lifetime in thin-film and multicrystalline photovoltaic materials," Sol. Energy Mater. Sol. Cells **94**(12), 2197–2204 (2010).

[20] H. Hempel, T. Unold, B. Rech, and T. Kirchartz, "Predicting solar cell performance from terahertz and microwave spectroscopy," Adv. Energy Mater. **12**(1), 2102776 (2022).

[21] J. Neu, "Optical pump terahertz probe (OPTP) and time resolved terahertz spectroscopy (TRTS) of emerging solar materials," APL Photon. **8**(7), 071103 (2023).

[22] G. Horowitz, P. Lang, M. Mottaghi, and H. Aubin, "Extracting parameters from the current-voltage characteristics of organic field-effect transistors," Adv. Funct. Mater. **14**(11), 1069–1074 (2004).

05 June 2026 18:55:54

© Author(s) 2026

[23]M. C. Beard, G. M. Turner, and C. A. Schmuttenmaer, "Transient photoconductivity in gaas as measured by time-resolved terahertz spectroscopy," Phys. Rev. B **62**(23), 15764 (2000).
[24]H. Ishii, K. Sugiyama, E. Ito, and K. Seki, "Energy level alignment and interfacial electronic structures at organic/metal and organic/organic interfaces," Adv. Mater. **11**(8), 605–625 (1999).
[25]L. S. Hung, C. W. Tang, and M. G. Mason, "Enhanced electron injection in organic electroluminescence devices using an Al/LiF electrode," Appl. Phys. Lett. **70**(2), 152–154 (1997).
[26]K. M. Ashikur Rahman, M. S. Shaikh, Q. Yue *et al.*, "Temperature-dependent dynamics of charge carriers in tellurium hyperdoped silicon," Adv. Electron. Mater. **11**, 2400417 (2024).
[27]S. H. Lee, K. Moon, M. Shoaib *et al.*, "Temperature-dependent recombination dynamics of photocarriers in $CsPbBr_3$ microcrystals revealed by ultrafast terahertz spectroscopy," Adv. Opt. Mater. **12**, 2401162 (2024).
[28]J. Neu and M. Rahm, "Terahertz time domain spectroscopy for carrier lifetime mapping in the picosecond to microsecond regime," Opt. Express **23**(10), 12900–12908 (2015).
[29]E. Butler-Caddle, N. E. Grant, S. L. Pain, and J. Lloyd-Hughes, "Terahertz photoconductance dynamics of semiconductors from sub-nanosecond to millisecond timescales," Appl. Phys. Lett. **122**(1), 012101 (2023).
[30]R. Lin, K. Xiao, Z. Qin, Q. Han, C. Zhang, M. Wei, M. I. Saidaminov, Y. Gao, J. Xu, M. Xiao, A. Li, J. Zhu, E. H. Sargent, and H. Tan, "Monolithic all-perovskite tandem solar cells with 24.8% efficiency exploiting comproportionation to suppress Sn(ii) oxidation in precursor ink," Nat. Energy **4**, 864–873 (2019).
[31]H. G. Roskos, M. D. Thomson, M. Kreß, and T. Löffler, "Broadband thz emission from gas plasmas induced by femtosecond optical pulses: From fundamentals to applications," Laser Photon. Rev. **1**(4), 349–368 (2007).
[32]F. A. Hegmann, O. Ostroverkhova, and D. G. Cooke, *Probing Organic Semiconductors with Terahertz Pulses* (Wiley Online Library, 2005), pp. 367–428.
[33]B. G. Alberding, W. R. Thurber, and E. J. Heilweil, "Direct comparison of time-resolved terahertz spectroscopy and Hall van der Pauw methods for measurement of carrier conductivity and mobility in bulk semiconductors," J. Opt. Soc. Am. B **34**(7), 1392–1406 (2017).
[34]T.-I. Jeon and D. Grischkowsky, "Nature of conduction in doped silicon," Phys. Rev. Lett. **78**(6), 1106 (1997).
[35]Y. U. Staechelin, T. Kroh, F. X. Kärtner, and H. Lange, "Impact of pump beam spot size on semiconductor carrier dynamics in optical-pump-terahertz-probe spectroscopy," J. Opt. Soc. Am. B **40**(8), 2058–2063 (2023).
[36]G. D. Smith, *Numerical Solution of Partial Differential Equations: Finite Difference Methods*, 3rd ed. (Oxford University Press, 1992).

05 June 2026 18:55:54

© Author(s) 2026